# 3D Dynamic Rupture Modeling of the 6 February 2023, Kahramanmaraş, Turkey $M_w$ 7.8 and 7.7 Earthquake Doublet Using Early Observations

Alice-Agnes Gabriel[*,1,2] ⓘ, Thomas Ulrich[2] ⓘ, Mathilde Marchandon[2] ⓘ, James Biemiller[3] ⓘ, and John Rekoske[1] ⓘ

## Abstract

The 2023 Turkey earthquake sequence involved unexpected ruptures across numerous fault segments. We present 3D dynamic rupture simulations to illuminate the complex dynamics of the earthquake doublet. Our models are constrained by observations available within days of the sequence and deliver timely, mechanically consistent explanations of the unforeseen rupture paths, diverse rupture speeds, multiple slip episodes, heterogeneous fault offsets, locally strong shaking, and fault system interactions. Our simulations link both earthquakes, matching geodetic and seismic observations and reconciling regional seismotectonics, rupture dynamics, and ground motions of a fault system represented by 10 curved dipping segments and embedded in a heterogeneous stress field. The $M_w$ 7.8 earthquake features delayed backward branching from a steeply branching splay fault, not requiring supershear speeds. The asymmetrical dynamics of the distinct, bilateral $M_w$ 7.7 earthquake are explained by heterogeneous fault strength, prestress orientation, fracture energy, and static stress changes from the previous earthquake. Our models explain the northward deviation of its eastern rupture and the minimal slip observed on the Sürgü fault. 3D dynamic rupture scenarios can elucidate unexpected observations shortly after major earthquakes, providing timely insights for data-driven analysis and hazard assessment toward a comprehensive, physically consistent understanding of the mechanics of multifault systems.

## Introduction

The destruction that unfolded in southeast Turkey and northwest Syria after the 6 February 2023, earthquake doublet (Fig. 1) was devastating. The first $M_w$ 7.8 earthquake was more than twice as large as the most significant known regional earthquakes, which had reached up to $M_w$ 7.4 (Fig. 1a; Duman and Emre, 2013), and is the most powerful earthquake recorded in Turkey since 1939. It initiated south of the Eastern Anatolian fault (EAF) on a splay fault known as the Nurdağı-Pazarcık fault (NPF) before branching northeast and southwest and bilaterally rupturing > 300 km of the EAF (Fig. 1a; Barbot *et al.*, 2023; Goldberg *et al.*, 2023; Jia *et al.*, 2023; Karabacak *et al.*, 2023; Mai *et al.*, 2023; Melgar *et al.*, 2023; Okuwaki *et al.*, 2023). The EAF did not host significant

earthquakes during the last century until the 2020 $M_w$ 6.8 Elaziğ earthquake (e.g., Cakir *et al.*, 2023), located north of the first rupture. Nine hours after the first earthquake, a second $M_w$ 7.7 earthquake ruptured the geometrically complex Çardak fault network ≈60 km north of the NPF–EAF junction. The

1. Scripps Institution of Oceanography, University of California San Diego, La Jolla, California, U.S.A., ⓘ https://orcid.org/0000-0003-0112-8412 (A-AG); ⓘ https://orcid.org/0000-0003-0539-2069 (JR); 2. Department of Earth and Environmental Sciences, Ludwig-Maximillians-Universität München, Munich, Germany, ⓘ https://orcid.org/0000-0002-4164-8933 (TU); ⓘ https://orcid.org/0000-0001-7883-8397 (MM); 3. U.S. Geological Survey, Portland, Oregon, U.S.A., ⓘ https://orcid.org/0000-0001-6663-7811 (JB)

*Corresponding author: algabriel@ucsd.edu
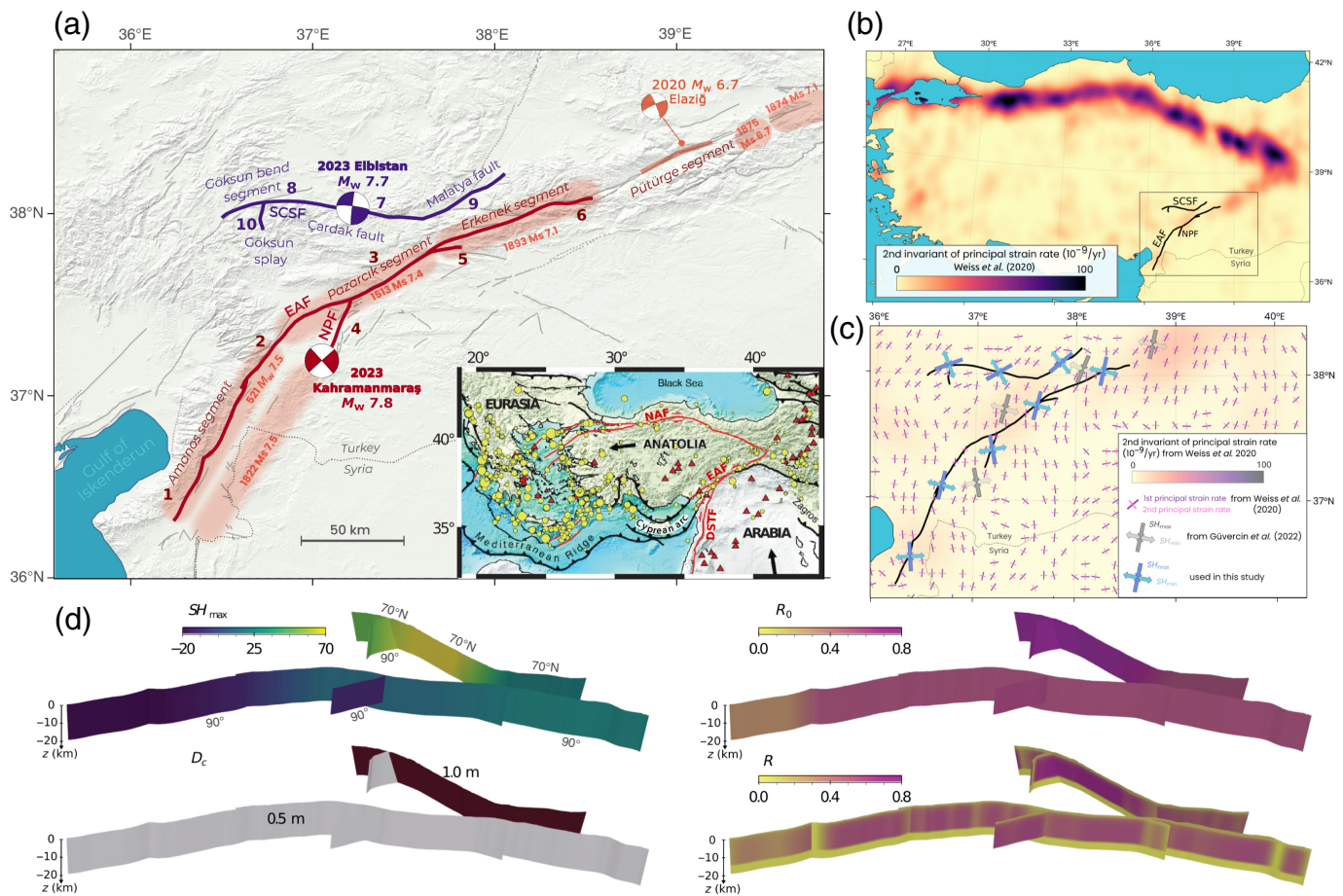
**Figure 1.** (a) Fault map with surface ruptures of the 2023 Turkey earthquake sequence. Focal mechanisms are from the U.S. Geological Survey (USGS; Goldberg et al., 2023). Shaded areas show the inferred extent of historic surface ruptures labeled by year and magnitude (Duman and Emre, 2013). Red and blue numbers correspond to fault segments modeled in this study named following Duman and Emre (2013). The first earthquake is modeled using six segments of the EAF: 1 and 2, Amanos segment; 3, Pazarcık segment; 4, Nurdağı-Pazarcık fault (NPF); 5, unnamed Erkenek splay; 6, Erkenek segment. The second earthquake ruptures four segments of the SCSF: 7, Çardak fault; 8, Göksun bend segment; 9, Malatya fault; and 10, unnamed Göksun splay. The Sürgü fault (segment 11) is shown in Figure 5. Inset shows regional tectonic map modified from Barbot and Weiss (2021). Yellow circles show earthquakes of $M_w > 3.0$ before 2021 (European-Mediterranean Seismological Centre [EMSC] catalog). DSTF, Dead Sea Transform fault; EAF, East Anatolian fault; NAF, North Anatolian fault; and SCSF, Sürgü–Çardak–Savrun fault. (b) Geodetically inferred second invariant of principal strain rate prior to the 6 February earthquakes from Weiss et al. (2020). The black rectangle outlines the area shown in the bottom panel. (c) Zoomed view of East Anatolian fault zone principal strain rate directions in purple (first component) and pink (second component) from Weiss et al. (2020). In dark and light gray, we show the seismologically inferred maximum and minimum principal horizontal stress components from Güvercin et al. (2022), as well as in dark and light blue, the maximum and minimum principal horizontal stress orientations used in this study. (d) Initial conditions for 3D dynamic rupture modeling of both large earthquakes. $SH_{max}[°]$ is the orientation of the maximum horizontal compressive stress from a new stress inversion we perform (based on Güvercin et al., 2022, Fig. S5), $D_c$ is the critical slip-weakening distance in the linear slip-weakening friction law, $R_0$ is the maximum relative prestress ratio, and $R < R_0$ is the fault-local relative prestress ratio modulated by varying fault geometry and orientation. Although the assumed $SH_{max}$ is the same in distinction to the dynamic rupture models in Jia et al. (2023), no additional smaller scale initial prestress or fault strength heterogeneity is prescribed.

Çardak fault is a part of the predominantly strike-slip Sürgü–Çardak–Savrun fault (SCSF) system, although the Sürgü segment, which connects the Çardak fault to the EAF, did not rupture.

The sequence ruptured segments of the northeast-striking EAF—a major intracontinental left-lateral strike-slip fault that accommodates northward convergence of the Arabian of the Arabian plate and westward motion of the Anatolian plate,

https://www.seismosoc.org/publications/the-seismic-record/ • DOI: 10.1785/0320230028 • *The Seismic Record* **343**

resulting in geologic and geodetic slip rates of up to 10 mm/yr across the complex EAF system (inset of Fig. 1a, Taymaz *et al.*, 2007; Duman and Emre, 2013; Weiss *et al.*, 2020). Ongoing approximately north–south Arabian–Eurasian collision squeezes and extrudes the Anatolian plate westward (Fig. 1a), driving westward migration and counterclockwise rotation of eastern Anatolia relative to Eurasia, along with transpression that is accommodated partly by intraplate distributed deformation and complex faulting, but primarily by slip along its major boundary faults: the right-lateral North Anatolian fault (NAF) to the north and the EAF to the southeast (e.g., Barbot and Weiss, 2021). The eastern SCSF branches to the west from the EAF and curves south to follow the EAF subparallel into the Gulf of Iskenderun to the southwest (Fig. 1a), where the SCSF links into the Cyprean Arc and a strand of the EAF continues south into the Dead Sea Transform fault (DSTF). Before hosting surprisingly large left-lateral coseismic slip on 6 February, the sense of offset along the SCSF remained debated (e.g., Koc and Kaymakçı, 2013; Duman and Emre, 2013), with fault-bounded geomorphologic features and slip orientations measured from fault scarps leading some to infer dextral motion (Koc and Kaymakçı, 2013).

The tectonic and structural complexity of the associated fault systems reflects the complex modern and paleotectonics of the region (Fig. 1a,b), highlighting how strain partitioning across distributed networks of nonuniformly oriented fault segments can accommodate sharp lateral variations in local tectonic loading (Duman and Emre, 2013; Weiss *et al.*, 2020; Barbot and Weiss, 2021; Güvercin *et al.*, 2022). The EAF is considered relatively immature compared to the NAF, initiating 2–5 Ma ago and since accruing 22–33 km of offset (Saroglu, 1992). Interferometric Synthetic Aperture Radar (InSAR) and Global Navigation Satellite System (GNSS) data show slightly elevated principal strain rates around the SCSF–EAF that are above interior Anatolian background levels but far lower than those along the NAF (Fig. 1b; Weiss *et al.*, 2020). Principal strain rate directions rotate ≈30° along the EAF from north-northwest near the Gulf of Iskenderun to north-northeast around the SCSF–EAF junction and northeast further along strike (Fig. 1b). Principal horizontal stress directions inverted from focal mechanisms of nearby earthquakes show similar ≈20°–30° clockwise rotations along the SCSF–EAF, from primarily north-northeast-trending in the southwest to northeast-trending near their intersection and further northeast (Fig. 1b). Similar to other recent significant earthquakes, such as the 2016 Kaikōura, New Zealand, earthquake and the 2019 Ridgecrest, California,

sequence, the 2023 Turkey earthquakes activated more fault segments than expected from geodetic slip rates and historical earthquakes, due to the geometrically complex fault structures interacting across space and time scales. These earthquakes illustrate the difficulties in reliable estimates of expected earthquake magnitudes due to short-term records, irregular cycles, and multifault rupture dynamics (Goldfinger *et al.*, 2013; Milner *et al.*, 2022).

Multiple slip episodes occurring close in time and activating fault segments nearby challenge data-driven analysis of large earthquakes. Initial imaging and data-driven modeling efforts based on strong motion, teleseismic, and high-rate GNSS data reveal dynamic and structural complexity of both the events, highlighted by opposing interpretations of fault system interaction and the characteristics of each earthquake, for example, the inferred local rupture speeds, activated fault segments, and seismic moment release. Joint data-driven interpretation using various geophysical and geologic datasets can illuminate the spatiotemporal evolution of the rupture sequence (e.g., Jia *et al.*, 2023) but typically cannot probe dynamically viable pre- and coseismic mechanical conditions. Detailed, physics-based interpretations can pose a unifying approach capable of explaining independent data sets and unifying unexpected field observations but are often only available on timescales of months to years after large earthquakes (e.g., Taufiqurrahman *et al.*, 2023). The complex interactions between various fault segments during multifault earthquake sequences can lead to more significant damage, complex seismic and geodetic data signatures, and modeling challenges, because they require considering the fault geometry and slip characteristics of multiple faults simultaneously.

We present 3D dynamic rupture models based on seismic and geodetic observations available within hours to days after the earthquakes. Our models are not initialized using solutions to inverse problems, such as a static slip model in the different simulations presented in Jia *et al.* (2023). We provide a new comparison of the fault offsets measured from Sentinel-2 displacement fields with the dynamic rupture models and compare the timing of the observed peak ground motions at unclipped strong-motion stations. Our models also explain the northward deviation of the second earthquake's western rupture and the minimal slip observed on the Sürgü segment. Our physics-based simulations disentangle the complex set of observations from the earthquake doublet and their interrelationship with general implications for the often-underestimated hazard from multifault rupturing

earthquakes. Furthermore, we highlight how quickly developed 3D dynamic rupture modeling constrained by observations available before and soon after complex ruptures can provide timely insight into the postseismic stress, strength, and rheological conditions of such fault systems, complementing post-event data collection and informing hazard estimation efforts.

## Methods

In data-driven kinematic models, a large number of free parameters enables close fitting of detailed observations, often at the expense of mechanical consistency and uniqueness of the solution. Dynamic rupture modeling involves simulating how earthquakes nucleate, propagate, and arrest. 3D models can directly reproduce geophysical and geologic observables, such as seismic waves, geodetic deformation patterns, and surface rupture patterns, in a physically self-consistent manner. Computational advances enable large-scale 3D dynamic rupture modeling informed by observations in various tectonic and scientific contexts. Such models require prescribed initial conditions, including fault geometry, fault strength, initial stress distribution, and material properties (Ramos *et al.*, 2022). Our 3D dynamic rupture simulations use the same spatially variable fault geometries, ambient tectonic loading, and fault strengths in a mechanically linked model of both the earthquakes that captures the respective effects of static and dynamic stress transfers during and between both the earthquakes. The basics of the dynamic rupture model setups and their computational cost (Fig. S7, available in the supplemental material to this article) are equivalent to the refined, more heterogeneous models of Jia *et al.* (2023). Our simulations allow us to analyze how the earthquakes are related by analyzing the conditions that contributed to the doublet occurrence, including fault geometry and mechanical properties. We base our model's initial conditions on a few parameters for which we can constrain their spatial variability from those observations available before and soon after the earthquakes, including fault geometry from space-geodesy and seismicity (see the Fault geometries section), fault loading from regional seismotectonics (see the Initial stresses and fault loading section), and dynamic parameters from observed earthquake kinematics such as moment rate release (see the Fault friction, off-fault plasticity, and dynamic fault strength section).

### Fault geometries

Our fault geometry includes 10 curved, intersecting segments with variable dip (Fig. 1d). We constrain the geometry of the

fault system from rupture traces mapped from coseismic horizontal surface displacements from pixel correlation of 10 m resolution Sentinel-2 satellite imagery (Table S3; Fig. S9; see Data and Resources). We show the coseismic east–west and north–south displacement fields and measured fault offsets in Figure 2. Our fault geometries capture large-scale geometrical complexities of the fault system, including fault bends, step-overs, and secondary segments. We extend the mapped surface fault traces to a depth of 20 km with varying dip angles ranging between 90° for the first earthquake's segments and 70° N for the main segments of the second earthquake, which is likely simplified but to first-order consistent with relocated aftershocks (Lomax, 2023). The small Göksun splay (segment 10) dips 90°. The revisit frequency of the Sentinel-2 optical or Sentinel-1 Synthetic Aperture Radar (SAR) satellite constellations is 5 and 6 days, respectively, implying that the surface rupture trace of a large continental earthquake can be constrained first order within this timeframe (see Fig. S9 for the optical displacement field we obtained 3 days after the doublet). We explore alternative models incorporating the Sürgü fault, which connects the SCSF to the EAF, with geometries constrained from geologic mapping (Emre *et al.*, 2018) in the Discussion section.

### Initial stresses and fault loading

We expose all fault segments to depth-dependent and laterally rotating initial stresses resembling the regional state of stress in the upper crust and regional stress inversion (Fig. 1d, Fig. S5). We combine the Mohr–Coulomb theory of frictional failure with dynamic parameters to reduce the ample parameter space of dynamic rupture modeling (e.g., Taufiqurrahman *et al.*, 2023). We construct a 3D Cartesian stress tensor $S_{ij}$ within the model domain (Fig. S7) from a new stress inversion we perform (based on Güvercin *et al.*, 2022, Fig. 1b, Fig. S5) for the orientation of the maximum horizontal compressive stress $SH_{max}$ and the stress shape ratio ν. The latter balances the amplitude of principal stress components and is here ν = 0.5, reflecting a strike-slip regime. We assume depth-dependent effective normal stress and overpressurized pore fluids. Above 6 km depth, we assume a pore fluid pressure ratio of $\gamma = \rho_{water}/\rho = 0.66$. At a larger depth, the pore fluid pressure gradient mirrors the lithostatic stress gradient, leading to constant effective normal stress below 6 km depth (Rice, 1992). There are few constraints on $SH_{max}$ near the seismically quiet Çardak fault (Fig. 1b). However, using a few trials of dynamic rupture simulations, we find that assuming along-strike rotating loading with
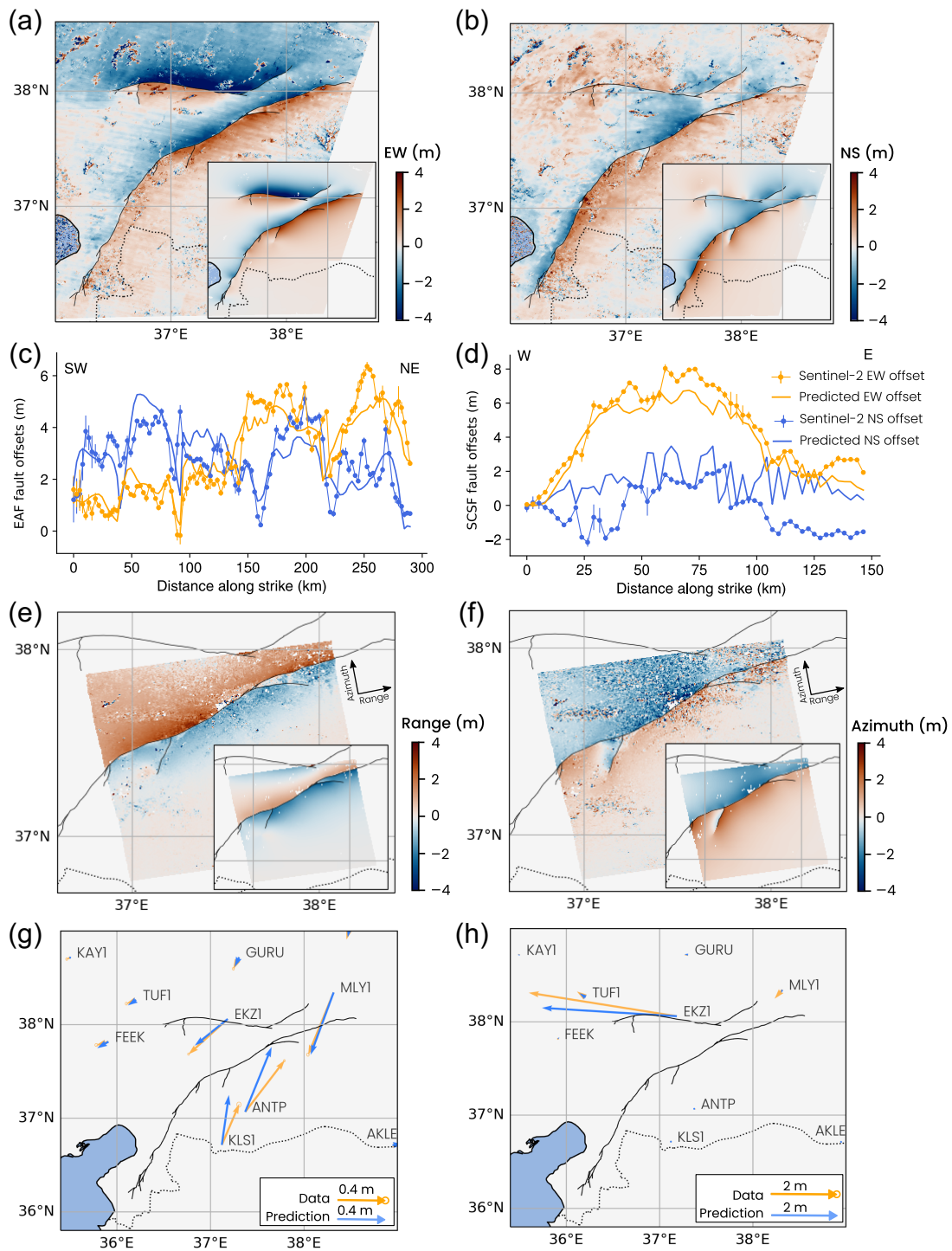
**Figure 2.** Comparison of the surface displacements predicted by our dynamic rupture models with various geodetic observations. (a,b) and (e,f) Comparison of Sentinel-2 east–west displacements, Sentinel-2 north–south displacements, RADARSAT-2 azimuth offsets, and RADARSAT-2 range offsets (see Data and Resources), respectively, with the model predictions shown in the inset of each panel. (c,d) Comparison of the fault offsets measured from the east–west and north–south Sentinel-2 displacement fields across the (c) $M_w$ 7.8 and (d) $M_w$ 7.7 ruptures with the fault offsets measured from the dynamic rupture models. See also Figure S9. (g,h) Comparison of observed (orange) and dynamic rupture modeled (blue) horizontal components of Global Navigation Satellite System (GNSS) displacements for the (g) $M_w$ 7.8 and (h) $M_w$ 7.7 earthquakes. The vector error ellipses represent a confidence interval of 95%.

close-to-optimal $SH_{max}$ close to the hypocenter of the second earthquake (Fig. 1d) is required to dynamically generate the observed large slip and surface displacements.

The relative prestress ratio $R$ of potential dynamic stress drop to full frictional breakdown strength is a crucial parameter controlling earthquake dynamics and dynamic triggering potential. We define

$$R = (\tau_0 - \mu_d \sigma_n)/[(\mu_s - \mu_d)\sigma_n], \tag{1}$$

in which $\tau_0$ and $\sigma_n$ are the initial shear and normal tractions on a fault plane, and $\mu_d$ and $\mu_s$ are the static and dynamic friction coefficients, respectively. $R$ governs the ratio of strain energy and fracture energy and, thus, determines local stress drop and acceleration or deceleration of the rupture front. Prescribing the maximum $R_0 \geq R$, as the relative prestress ratio of an optimally oriented fault portion, allows us to constrain deviatoric stress amplitudes by balancing the amplitude of prestress relative to the frictional strength drop. We find that the observed complexities of the first and the second earthquake require $R_0$ to be variable within the model domain.

The relative prestress ratio of an optimally oriented fault in the complex stress field, which is first-order aligned with regional rotations of principal stress directions, ranges between $R_0 = 0.3...0.8$ (Fig. 1d, Fig. S5). Local fault geometry further modulates fault prestress and strength, resulting in heterogeneous fault-local $R \leq R_0$, and implying that locally more optimally oriented fault portions are closer to critically prestressed. Our parameterization satisfies the dynamic constraints that the second earthquake's fault structure is not dynamically triggered during the first earthquake rupture in our linked simulations. As we show in the Discussion section, these tectonically constrained prestress and fault strength conditions also explain why the Sürgü fault did not coseismically slip during the second earthquake, without requiring choosing locally different conditions. Importantly, we must prescribe larger fracture energy and larger nucleation energy in addition to dynamically stronger main faults for the second earthquake to capture their distinct rupture dynamics, as explained in the next section.

## Fault friction, off-fault plasticity, and dynamic fault strength

We demonstrate that simple friction parameters can give rise to the distinct slip characteristics of both the earthquakes, and promote dynamic and static multifault earthquake cascading in complex tectonic contexts. We use the widely used linear slip-weakening friction law (Andrews, 1976), which we parameterize with static friction coefficient $\mu_s = 0.6$ and dynamic friction coefficient $\mu_d = 0.2$ (Table S2). The critical slip distance varies between $D_c = 0.5$ m for faults hosting the first earthquake and larger $D_c = 1.0$ m, implying larger fracture energy, for the main faults hosting the second earthquake. All faults will begin to slip when shear stresses locally exceed the high-static frictional fault strength. Fault strength then decreases linearly from static to dynamic levels over the critical slip distance. We assume a depth-dependent, nonassociated Drucker–Prager elasto-viscoplastic rheology to model coseismic off-fault plastic deformation. Off-fault plasticity is parameterized by bulk internal friction coefficient and 1D variable plastic cohesion. We use a uniform bulk friction coefficient of 0.6, matching our on-fault static friction coefficient, and define plastic cohesion $C_{plast}$ as proportional to the 1D depth-dependent shear modulus (Table S1).

We link both the dynamic rupture earthquake models in the same simulation to account for the dynamic and static stress changes. To this end, we initiate the second earthquake at 150 s simulation time after initiating the first earthquake to ensure that no significant wave-transmitted dynamic stresses of the first earthquake interfere with the second dynamic rupture simulation. We do not account for potential interseismic aseismic slip or healing. We use nucleation patches that grow smoothly in time and across a minimal-sized perturbation area, reproducing rupture kinematics determined in several trial dynamic rupture simulations. The nucleation radius must be chosen larger for the second earthquake than the first, despite the second fault system being closer to critical prestress levels: Nucleation patch sizes are 2 km and 3 km for the $M_w$ 7.8 and 7.7 earthquakes, respectively.

## Results

Our linked dynamic rupture scenarios of the $M_w$ 7.8 and 7.7 doublet are each dynamically consistent with respective seismic and geodetic observations and the observed rupture patterns and fault-system interaction. We summarize the modeled rupture dynamics of both the earthquakes in Figure 3, and compare them with geodetic and near-field seismic observations in Figures 2 and 4. Although the slip distributions resulting from these simpler models are smoother, rupture dynamic results are generally consistent with more heterogeneous models (Fig. S6; Jia et al., 2023), demonstrating the robustness of our results and the extent to which broad crustal mechanical

Figure 3. The 3D dynamic rupture scenarios of the $M_w$ 7.8 and 7.7 earthquakes. (a) Snapshots of absolute slip rate of the $M_w$ 7.8 dynamic rupture scenario (see also Videos S1, S3). The earthquake activates faults 1–6 but does not coseismically trigger faults 7–10 nor 11 (Fig. 5), which we include in the same simulation. (b) Total fault slip (first row), dip-component of fault slip (second row), peak slip rate (third row), and rupture speed (fourth row) of both dynamic rupture models. (c) Snapshots of absolute slip rate of the $M_w$ 7.7 dynamic rupture scenario (see also Videos S2, S4). The model breaks faults 7–10, which are in addition to the ambient prestress (Fig. S5) affected by the stress changes of the earlier $M_w$ 7.8 dynamic rupture. (d) Dynamic rupture moment release rates of the $M_w$ 7.8 (top) and the $M_w$ 7.7 (bottom) earthquakes compared to kinematic models (Goldberg et al., 2023; Melgar et al., 2023; Okuwaki et al., 2023) and more heterogeneous dynamic rupture models (Jia et al., 2023). The dynamically unfavorable fault system configuration causes a pronounced delay before the EAF ruptures in the backward direction to the southwest. Color bars are not saturated and reflect fault-local maximum values; for example, the maximum local peak slip rate is 8.8 m/s during the $M_w$ 7.8 and 9.1 m/s for the $M_w$ 7.7 simulation.

conditions established by regional seismotectonics may control notable features of the rupture sequence evolution.

## Rupture dynamics of the $M_w$ 7.8 earthquake

The $M_w$ 7.8 dynamic rupture scenario shows three distinct rupture phases. Rupture is artificially nucleated (Fig. 3) and starts as a subshear crack-like rupture on the NPF—an north-northeast-striking splay fault south of the EAF. After this first rupture episode, the geometric barrier formed by the NPF–EAF intersection nearly arrests the rupture (Fig. S2), leading to temporarily negligible seismic moment release rates. This delay is stable for different initial conditions (i.e., is also observed in alternative rupture models in Jia et al., 2023 and Fig. 5) and corresponds to a pronounced trough in teleseismically inferred moment rate release at 18 s rupture time (Fig. 3d)

**Figure 4.** (a,b) Comparison of modeled and observed strong ground motions for both the earthquakes. Synthetic (purple = $M_w$ 7.8, blue = $M_w$ 7.7, gray = more heterogeneous dynamic rupture models (Fig. S6, Jia *et al.*, 2023) and observed (black, AFAD) ground velocity time series at near-fault strong-motion stations shown in the insets, band-pass filtered between 0.01 and 1 Hz. No amplitude scaling or time shifts are applied. The numbers on the top left of each waveform are cross-correlation coefficients with observations. (c.d). Map of the observed peak ground velocity (PGV) measurements (AFAD, see Data and Resources) at unclipped strong-motion stations that recorded the (c) $M_w$ 7.8 and (d) $M_w$ 7.7 earthquakes. The size of the circles indicates the PGV value, and the colors indicate the time at which the PGV occurred. The simulated waveforms in the dynamic rupture models resolve frequencies of at least 1 Hz close to the fault system (Fig. S7). PGV is here computed as $\sqrt{PGV_xPGV_y}$. For a color-coded comparison of PGV amplitudes and quantification of the differences in PGV timing and amplitudes, see Figure S8. We account for topography, viscoelastic attenuation, and off-fault plasticity but use a 1D model of subsurface structure (Table S1).

and a delay in observed peak ground velocities (PGVs) after rupture onset (Fig. 4c, Fig. S8).

Crack-like rupture branching in the forward direction (toward the northeast) dominates the second rupture phase, whereas rupture branching to the southwest is dynamically unfavorable and causes a pronounced delay before the third rupture phase. The forward direction branch of the EAF is oriented at ≈145° to the NPF, which is close to optimal rupture branching angles (Kame et al., 2003). Although forward-direction branching to the northeast is expected to be mechanically favorable, direct backward branching of the same slip style as the main rupture (i.e., here, left-lateral) is unexpected and theoretically unfavorable; the main rupture is expected to induce shear stress in the opposite rake direction on the backward branch, impeding rupture there (e.g., Poliakov et al., 2002; Fliss et al., 2005). Therefore, backward branching at ≈35° is discouraged under all prestress conditions in theoretical and numerical analysis accounting for the dynamic stress field at the rupture front. However, backward branching has been observed in real earthquakes such as the Landers earthquake, the Hector Mine earthquake, and the Romanche transform fault earthquake. To explain these observations, complex mechanisms, including rupture jumping, delayed reactivation of weakened faults, free-surface interactions, and 3D prestress or locking heterogeneities have been suggested (Kame et al., 2003; Oglesby et al., 2003; Fliss et al., 2005; Wollherr et al., 2019; Hicks et al., 2020). Our findings agree with these previous static and dynamic analyses in that immediate bilateral dynamic rupture branching to both sides of the EAF is dynamically unfavorable. However, we show that 3D dynamic effects, including progressive unclamping, transient shear stressing, and static stress build-up at the fault intersection and the southwest branch itself (Fig. S2) due to the propagating northeast rupture, eventually lead to delayed and self-sustained branching toward the southwest. This mechanism is simpler than rupture jumping, free-surface effects, or 3D prestress variability.

In the third phase of the dynamic model, two bilateral pulse-like rupture fronts, with strong directivity and median rupture speeds of 3 km/s, unzip the EAF in both the directions. Figure 3b illustrates the modeled fault slip reaching up to 8.2 m on the Erkenek segment. We observe shallow dip-slip components due to dynamic rake changes enhanced near the free surface where confining stresses are low. Rupture speed remains overall subshear during the first earthquake.

Our dynamic rupture scenario reproduces various geodetic observations, including SAR and GNSS offsets, and optical correlation data of the first earthquake (Fig. 2a,b,c,e,g). In particular, the predicted fault offsets fit observations remarkably well (Fig. 2c), demonstrating that our model matches the surface slip amplitude variations due to fault system segmentation. The model also reproduces the timing and amplitude of the impulsive strong ground motion signals recorded at stations along the fault to first order (Fig. 4a), which are generated due to a combination of surface rupture, partially pulse-like rupture, and strong directivity. Our models show that intense near-field pulses (Fig. 5, e.g., station 4615) can be caused by surface-breaking subshear strike-slip rupture as well as by supershear rupture (see the Discussion section).

## Rupture dynamics of the $M_w$ 7.7 earthquake

Rupture of the $M_w$ 7.8 earthquake does not coseismically trigger sustained coseismic slip along the second earthquake's fault system (Fig. S1a). However, the static stress changes due to the first earthquake bring its central segments closer to failure while considerably shadowing its eastern regions (Fig. S1b). Despite the compound rupture extent, our modeled rupture dynamics are strongly asymmetric, and feature westward supershear rupture speeds and eastward subshear rupture (Fig. 3c). In comparison to the first earthquake, the modeled fault slip (up to 9.4 m, Fig. 3b) and stress drop (Fig. S3) are considerably larger, whereas peak slip rates are lower, reflecting differences in prestress and fracture energy ($D_c$, Fig. 1d) between these scenarios. Figure S4 shows an alternative simulation of the second earthquake without accounting for the change in Coulomb failure stress (ΔCFS, Fig. S1b) of the first earthquake. In the east, where the stress shadow of (negative) ΔCFS is the largest, the second earthquake's rupture speed, slip amplitude, and peak slip rate are considerably increased (Fig. S4c). In distinction, fault slip is smaller on the central segment for which ΔCFS is positive (9.2 m). The static stress changes due to the first earthquake moves the second earthquake's eastern segments away from failure, aiding asymmetry between westward and eastward rupture dynamics, and increasing peak slip.

As in the preceding $M_w$ 7.8 earthquake, the combined dynamic rupture model synthetics closely match the Sentinel-2 surface displacement field (Fig. 2a) and the east–west fault offsets (Fig. 2d) of the second earthquake. Both the dynamic rupture earthquake scenarios also largely match the amplitude of the horizontal displacement direction at site EKZ1 (the GNSS station closest to the second earthquake) with slight differences in orientation (Fig. 2g). The mismatch for the
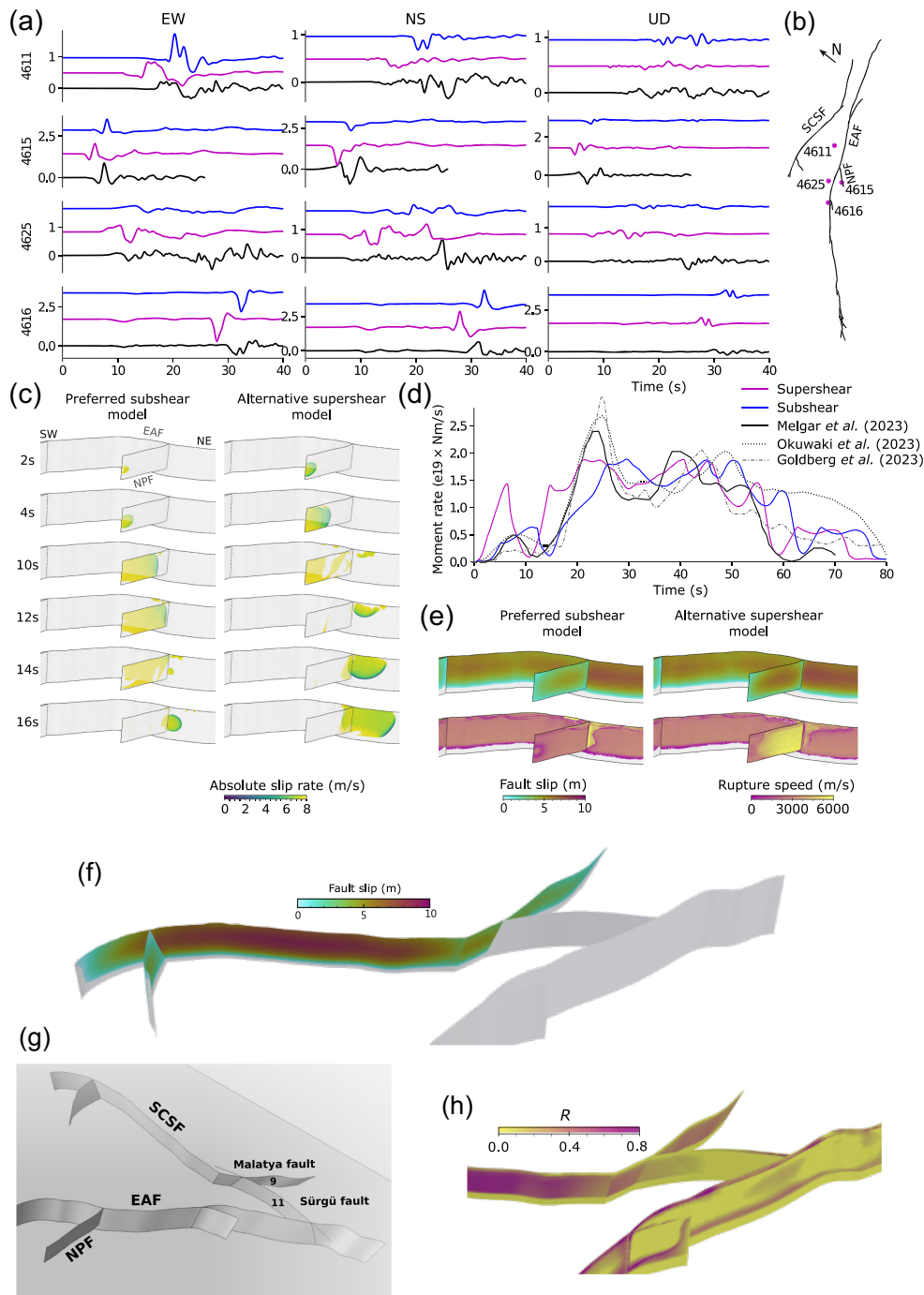
**Figure 5.** (a–e) Alternative dynamic rupture scenarios for the first and (f–h) second earthquake. (a–e) Supershear rupture on the first segment (NPF) of the $M_w$ 7.8 earthquake compared to our preferred subshear model. (a,b) Strong ground motions, (c) slip-rate evolution, (d) moment rate release, fault slip, and (e) rupture speed close to the NPF–EAF intersection. (f–h) Dynamic rupture model of the $M_w$ 7.7 earthquake when the Sürgü connecting fault, or Doğanşehir segment, between the fault systems of the first and second earthquake, is added as the 11th fault. (f) Nonrupture of the Sürgü fault, which is not triggered. The resulting slip on all other faults hosting the second earthquake is the same as in our preferred 10-segment model. (g) We constrain the Sürgü fault geometry from the active fault database (Emre *et al.*, 2018) using a dip of 70° and $D_c = 0.5$ m while keeping all other model parameters the same (Fig. 1). We explored a change in the dip of the connecting Sürgü segment to 90° (not shown), which led to equivalent dynamic rupture results. (h) The segment-local unfavorable relative prestress ratio $R$ resulting from our regional stress model and fault geometries, preventing the second earthquake's rupture connecting to the EAF during the $M_w$ 7.7 dynamic rupture scenario.

eastward north–south offsets of the second earthquake may imply that either the assumed dip angle of this fault segment is too shallow, the modeled dip-slip component is too large, or both.

Few near-source recordings are available for the second earthquake, challenging model verification with strong ground motion. Our synthetics capture the shape and amplitude of recorded ground-motion pulses reasonably well (Fig. 4b). The fit with the timing and amplitudes of observed PGV is good (Fig. S8), which supports our fault stress and strength assumptions differing for the second earthquake: assuming larger fracture energy and more critically stressed faults lead to larger stress drop (Fig. S3) but does not cause larger PGVs. In distinction, the high but subcritical EAF prestress, governing the first earthquake results in delayed backward branching, and rupture are unable to immediately activate the fault system of the second earthquake.

## Discussion

### Unexpected doublet dynamics explained by stress and strength heterogeneity

The dynamic stressing around a propagating rupture is enhanced with increasing rupture velocity and may drive rupture across steep branching angles, as discussed in Kame *et al.* (2003), for varying

sub-Rayleigh rupture speeds. Motivated by this, Figure 5a–e explores dynamic rupture scenarios featuring supershear versus subshear rupture speeds on the NPF during the $M_w$ 7.8 earthquake. Both overcome the geometric barrier (Fig. S2) and are difficult to distinguish in near-fault ground-motion synthetics. Although the supershear Mach front promotes rupture jumping, the dominant driving factor aiding subshear rupture branching from the NPF to the EAF is the abrupt stopping of surface-breaking strike-slip rupture at the geometric barrier (Fig. S2, Fliss et al., 2005). In both the cases, the abrupt stopping of the first rupture at the intersection of the hypocentral NPF with the EAF causes a clear delay in the moment release rate and aids rupture branching to the northeast of the EAF. The varying mechanisms involve equally delayed activation of a shallower part of the western EAF. We do not explore models featuring local eastward supershear rupture in the second phase of the first earthquake, at the EAF after the NPF–EAF junction (Wang et al., 2023), which may improve moment rate release match at 25 s rupture time.

The $M_w$ 7.7 rupture deviated northward in this model (and in Jia et al., 2023), breaking the Malatya fault (Fig. 5g), instead of connecting across the Sürgü or Doğanşehir fault to the EAF (as suggested by Melgar et al., 2023). We include this fault as an 11th segment in an alternative scenario of the second earthquake, keeping other model parameters unchanged. Surprisingly, the second rupture does not trigger the now included Sürgü fault coseismically (Fig. 5f–h), and the dynamics of the sharp deviation are unaffected, despite static stress changes favoring a straight rupture path (Fig. S1b, Jia et al., 2023), and without added heterogeneity. Segment 11 is poorly aligned to our regional stress field resulting in a lower subcritical prestress ($R \leq 0.2$) than the Malatya fault. The large coseismic stresses from the propagating rupture and radiating seismic waves (Fig. S1) cannot overcome these barriers nor trigger even minor-to-moderate slip.

Larger fracture energy and more critically stressed faults of the SCSF system (Fig. 1, Fig. S5) are required to model the compound, supershear rupture, and higher stress drop of the second earthquake (Fig. 3, Fig. S3). This may reflect dynamically triggered fault valving due to upwelling fluids (Sibson, 1992) or locally more immature fault structures than the EAF, however, supershear rupture is generally assumed to be favored by more mature faults (Perrin et al., 2016). Distributed faulting and deformation across subparallel strands and splays of the SCSF–EAF suggest that these complex fault systems may have initiated and developed in response to relatively recent changes in regional tectonic loading, compared to potentially steadier loading responsible for long-lived and highly localized slip on the northeast portion of the EAF. Although the SCSF includes reactivated Miocene structures (e.g., Duman and Emre, 2013), its diffuse and complex geometry suggests that it may be effectively less mature than the well-developed EAF.

Regional strain partitioning across complex faults may predispose local and complex fault-to-fault stress interactions that prevent steady, long-term slip (Fletcher et al., 2016) but favor cascading earthquake dynamics and sequences. An evident lack of seismicity at the SCSF after the 2020 Elaziğ earthquake as well as after the 2023 $M_w$ 7.8 earthquake (Lomax, 2023) supports differences in dynamic fault strength. As a result, both the rupture scenarios feature surprisingly different and distinct earthquake dynamics that are difficult to incorporate into earthquake hazard assessment: The $M_w$ 7.8 grew larger than expected due to the dynamic breaching of geometric barriers, including branching into steep backward direction considered mechanically unfavorable. The $M_w$ 7.7 scenario features local supershear rupture on a dynamically stronger fault segment than those hosting subshear rupture during the first earthquake.

## Unlocking the keystones of multifault ruptures

Because our dynamic rupture simulations necessitate relatively high but subcritical initial prestress on the EAF to correspond with the observed slip patterns in the first earthquake, we hypothesize that the EAF could be an "imperfect keystone" fault for southeast Turkey (Fletcher et al., 2016), governing the overall strength and eventual multisegment failure of a complex fault system. Smaller intersecting or neighboring faults, such as the NPF, may reach critical stress states from tectonic loading before the keystone fault, subsequently dissipating strain energy through minor slip during the keystone fault's late interseismic period and remaining "pinned" and unable to rupture until the keystone fault nears failure.

Our models illustrate the predisposition of complex fault geometries, prevalent in tectonically complex immature fault systems, for cascading multifault and multievent earthquake sequences. The Turkey–Syria doublet and other recent large earthquakes involving multifault rupture sequences highlight how understanding their underlying mechanics is crucial to improving earthquake hazard assessment and mitigation. Geometrically complex fault systems are often immature or located in regions of complex or recently reoriented tectonic

loading, implying that the complexity of our presented scenarios may not be unusual. Identifying and characterizing potential keystone faults conjointly with local prestress may help improve hazard estimates for complex fault networks and constrain key inputs to dynamic rupture simulations.

### Toward "rapid" dynamic rupture modeling

Our results demonstrate that regionally constrained and simple dynamic rupture scenarios are capable of matching important characteristics relevant for earthquake engineering: our physics-based earthquake scenarios resolving up to 1 Hz seismic-wave propagation (Fig. S7) match the timing of observed near-fault PGVs and near-fault ground-motion velocity pulses (Fig. 4, Fig. S8). We do not solve inverse problems nor use solutions to inverse problems to initialize our models but validate 3D dynamic rupture forward simulations with regional observations retrospectively. Our modeled slip distributions (Fig. 3b) are relatively smooth, result in a larger moment of the first earthquake, and have slightly worse geodetic misfit (by 2.2%, Fig. S6) than in Jia *et al.* (2023). A potential explanation is that our initial conditions do not account for smaller scale heterogeneities, such as local prestress or fault strength asperities, along-strike variations in seismogenic depth, higher variability of pore fluid pressure, and 3D subsurface structure. Both dynamic rupture models, simple and refined, do not match all observed waveform complexities (Figs. 4a,b, 5), which may be due to unaccounted local acceleration and deceleration of the rupture front due to fault segmentation or roughness, frictional or stress heterogeneities, off-fault damage and scattering by structural heterogeneities.

This study models both earthquakes together, which limits the typically vast parameter space of initial conditions for dynamic rupture simulations (Harris, 2004; Ramos *et al.*, 2022) in a self-consistent manner (Taufiqurrahman *et al.*, 2023). For instance, this approach enforces the same regional background stress conditions at the connection of both fault systems and constraints fault strength (relative prestress ratio) to avoid the dynamic triggering of segments that did not slip while reproducing rupture dynamics where slip occurred. Directly constraining remaining uncertainties would require denser observations (e.g., Ben-Zion *et al.*, 2022). However, the models can, based on their self-consistency and the achieved fit to observational data, serve as strong first-order constraints of the doublet's mechanics. They can also serve as a base for refined dynamic rupture simulations to which additional data inferences can be added as they become available. These can be from static,

kinematic, or dynamic slip inversion models, for example, using a Bayesian approach as for the 2020 Elaziğ earthquake (Gallovič *et al.*, 2020).

Joint observing and modeling of the long- and short-term, dynamic, and static earthquake interactions are crucial for seismic hazard assessment of active multifault systems to overcome the resulting challenges to empirical hazard assessment and rapid response efforts. For example, joint mapping and seismological analyses may help validate our imperfect keystone hypothesis by determining pre- and postsequence crustal stresses. Combined with dynamic rupture modeling, static and dynamic mechanical inferences could inform rapid assessments of the likelihood of triggering of fault segments within and near a main ruptured fault system by helping estimate the spatial distributions of maximum dynamic stress perturbations from both the earthquakes, the net static stress changes from the rupture sequence, and the relative strengths of different fault segments subject to the local tectonic stress field.

## Conclusions

We show that structurally and geodetically informed fault geometries, regional seismotectonics, and early observations typically available within hours to days after large crustal earthquakes (Lacassin *et al.*, 2020) are sufficient constraints to enable meaningful postevent dynamic rupture modeling. Our results have implications for seismic hazard assessment: large multifault earthquakes commonly exhibit seemingly unexpected rupture behaviors, which may be explained by dynamic and static stress transfers between variably oriented fault segments in 3D variable tectonic environments. Unexpected slip patterns and their associated hazards are dynamically plausible, and may be a typical, expected behavior specifically for ruptures of complex immature multifault systems. High stress-drop events may be triggered in geometrically complex fault systems. A single fault system with variable relative strength can host dynamic rupture propagating at highly variable sub-to-supershear rupture speeds across different segments and in different directions, including branching and delayed triggering in backward direction.

## Data and Resources

The three-component coseismic displacements recorded by Global Positioning System (GPS) stations of the CORS network (https://geodesy.noaa.gov/CORS/) have been downloaded from the Nevada Geodetic Laboratory website (http://geodesy.unr.edu/). Sentinel-1 Synthetic Aperture

Radar (SAR) offsets are processed by the National Aeronautics and Space Administration's (NASA) Jet Propulsion Laboratory (JPL) and the California Institute of Technology (Caltech) available at https://aria-share.jpl.nasa.gov/20230206_Turkey_EQ/Displacements/Sentinel1/. The European-Mediterranean Seismological Centre (EMSC) catalog is accessible at www.seismicportal.eu. The Sentinel-2 optical images are freely available and were downloaded from the European Space Agency website (https://scihub.copernicus.eu/dhus/#/home). We obtained strong ground motion data from the Turkish National Strong Motion Network through the Disaster and Emergency Management Presidency of Türkiye (AFAD, https://tadas.afad.gov.tr). All data required to reproduce the earthquake doublet dynamic rupture scenarios, including the manuscript figures, can be downloaded from https://github.com/Thomas-Ulrich/Turkey-Syria-Earthquakes. We illustrate our stress inversion method in a Jupyter Notebook available at https://zenodo.org/doi/10.5281/zenodo.10058942. All dynamic rupture simulations were performed using SeisSol (www.seissol.org)—an open-source software freely available to download from https://github.com/SeisSol/SeisSol/. We use SeisSol, commit 234fad5 (master branch on 21 March 2023). Instructions for downloading, installing, and running the code are available in the SeisSol documentation at https://seissol.readthedocs.io/. Downloading and compiling instructions are at https://seissol.readthedocs.io/en/latest/compiling-seissol.html. Instructions for setting up and running simulations are at https://seissol.readthedocs.io/en/latest/configuration.html. Quickstart containerized installations and introductory materials are provided in the docker container and Jupyter Notebooks at https://github.com/SeisSol/Training. Example problems and model configuration files are provided at https://github.com/SeisSol/Examples, many of which reproduce the Southern California Earthquake Center (SCEC) 3D Dynamic Rupture benchmark problems described at https://strike.scec.org/cvws/benchmark_descriptions.html. All websites were last accessed in November 2023.

## Declaration of Competing Interests

The authors acknowledge that there are no conflicts of interest recorded.

## Acknowledgments

Any use of trade, firm, or product names is for descriptive purposes only and does not imply endorsement by the U.S. Government.

## References

Andrews, D. (1976). Rupture propagation with finite stress in antiplane strain, *J. Geophys. Res.* **81,** no. 20, 3575–3582.

Barbot, S., and J. Weiss (2021). Connecting subduction, extension and shear localization across the Aegean Sea and Anatolia, *Geophys. J. Int.* **226,** no. 1, 422–445.

Barbot, S., H. Luo, T. Wang, Y. Hamiel, O. Piatibratova, M. T. Javed, C. Braitenberg, and G. Gurbuz (2023). Slip distribution of the February 6, 2023 Mw 7.8 and Mw 7.6, Kahramanmaraş, Turkey earthquake sequence in the East Anatolian Fault Zone, *Seismica* **2,** no. 3, doi: 10.26443/seismica.v2i3.502.

Ben-Zion, Y., G. C. Beroza, M. Bohnhoff, A. Gabriel, and P. M. Mai (2022). A grand challenge international infrastructure for earthquake science, *Seismol. Res. Lett.* **93,** no. 6, 2967–2968, doi: 10.1785/0220220266.

Cakir, Z., U. Doğan, A. M. Akoğlu, S. Ergintav, S. Özarpacı, A. Özdemir, T. Nozadkhalil, N. Çakir, C. Zabcı, M. H. Erkoç, *et al.* (2023). Arrest of the Mw 6.8 January 24, 2020 Elaziğ (Turkey) earthquake by shallow fault creep, *Earth Planet. Sci. Lett.* **608,** 118085, doi: 10.1016/j.epsl.2023.118085.

Duman, T. Y., and Ö. Emre (2013). *The East Anatolian Fault: Geometry, Segmentation and Jog Characteristics*, Vol. 372, Geological Society, London, Special Publications, 495–529, doi: 10.1144/SP372.14.

Emre, Ö., T. Y. Duman, S. Özalp, F. Şaroğlu, Ş. Olgun, H. Elmacı, and T. Çan (2018). Active fault database of Turkey, *Bull. Earthq. Eng.* **16,** no. 8, 3229–3275.

Fletcher, J. M., M. E. Oskin, and O. J. Teran (2016). The role of a keystone fault in triggering the complex El Mayor-Cucapah earthquake rupture, *Nature Geosci.* **9,** no. 4, 303–307.

Fliss, S., H. S. Bhat, R. Dmowska, and J. R. Rice (2005). Fault branching and rupture directivity, *J. Geophys. Res.* **110,** no. B6, doi: 10.1029/2004JB003368.

Gallovič, F., J. Zahradník, V. Plicka, E. Sokos, C. Evangelidis, I. Fountoulakis, and F. Turhan (2020). Complex rupture dynamics on an immature fault during the 2020 Mw 6.8 Elazığ earthquake, Turkey, *Commun. Earth Environ.* **1,** no. 1, 40.

Goldberg, D. E., T. Taymaz, N. G. Reitman, A. E. Hatem, S. Yolsal-Çevikbilen, W. D. Barnhart, T. S. Irmak, D. J. Wald, T. Öcalan, W. L. Yeck, et al. (2023). Rapid characterization of the February 2023 Kahramanmaraş, Türkiye, earthquake sequence, *Seismic Record* **3,** no. 2, 156–167, doi: 10.1785/0320230009.

Goldfinger, C., Y. Ikeda, R. S. Yeats, and J. Ren (2013). Superquakes and supercycles, *Seismol. Res. Lett.* **84,** no. 1, 24–32.

Güvercin, S. E., H. Karabulut, A. Ö. Konca, U. Doğan, and S. Ergintav (2022). Active seismotectonics of the East Anatolian Fault, *Geophys. J. Int.* **230,** no. 1, 50–69.

Harris, R. A. (2004). Numerical simulations of large earthquakes: Dynamic rupture propagation on heterogeneous faults, in *Computational Earthquake Science Part II*, A. Donnellan, P. Mora, M. Matsu'ura, and Xc. Yin (Editors), PAGEOPH Topical Volumes, Birkhäuser, Basel, 2171–2181, doi: 10.1007/978-3-0348-7875-3_5.

Hicks, S. P., R. Okuwaki, A. Steinberg, C. A. Rychert, N. Harmon, R. E. Abercrombie, P. Bogiatzis, D. Schlaphorst, J. Zahradnik, J. M. Kendall, et al. (2020). Back-propagating supershear rupture in the 2016 Mw7.1 Romanche transform fault earthquake, *Nature Geosci.* **13,** no. 9, 647–653.

Jia, Z., Z. Jin, M. Marchandon, T. Ulrich, A. A. Gabriel, W. Fan, P. Shearer, X. Zou, J. Rekoske, F. Bulut, et al. (2023). The complex dynamics of the 2023 Kahramanmaraş, Turkey, Mw 7.8-7.7 earthquake doublet, *Science* **381,** no. 6661, 985–990, doi: 10.1126/science.adi0685.

Kame, N., J. R. Rice, and R. Dmowska (2003). Effects of prestress state and rupture velocity on dynamic fault branching, *J. Geophys. Res.* **108,** no. B5, doi: 10.1029/2002JB002189.

Karabacak, V., Ç. Özkaymak, H. Sözbilir, O. Tatar, B. Aktuğ, Ö. C. Özdağ, R. Çakir, E. Aksoy, F. Koçbulut, and M. Softa et al. (2023). The 2023 Pazarcık (Kahramanmaraş, Türkiye) earthquake ($M_w$ 7.7): Implications for surface rupture dynamics along the East Anatolian Fault Zone, *J. Geol. Soc.* **180,** no. 3, doi: 10.1144/jgs2023-020.

Koc, A., and N. Kaymakcı (2013). Kinematics of Sürgü fault zone (Malatya, Turkey): A remote sensing study, *J. Geodynam.* **65,** 292–307.

Lacassin, R., M. Devès, S. P. Hicks, J. P. Ampuero, R. Bossu, L. Bruhat, D. F. Wibisono, L. Fallou, E. J. Fielding, and A. A. Gabriel (2020). Rapid collaborative knowledge building via twitter after significant geohazard events, *Geosci. Commun.* **3,** no. 1, 129–146.

Lomax, A. (2023). Precise, NLL-SSST-coherence hypocenter catalog for the 2023 Mw 7.8 and Mw 7.6 SE Turkey earthquake sequence, *Zenodo* doi: 10.5281/zenodo.7699882.

Mai, P. M., T. Aspiotis, T. A. Aquib, E. V. Cano, D. Castro-Cruz, A. Espindola-Carmona, B. Li, X. Li, J. Liu, R. Matrau, et al. (2023). The destructive earthquake doublet of 6 February 2023 in South-Central Türkiye and Northwestern Syria: Initial observations and analyses, *Seismic Record* **3,** no. 2, 105–115, doi: 10.1785/0320230007.

Melgar, D., T. Taymaz, A. Ganas, B. W. Crowell, T. Öcalan, M. Kahraman, V. Tsironi, S. Yolsal-Çevikbil, S. Valkaniotis, T. S. Irmak, et al. (2023). Sub-and super-shear ruptures during the 2023 Mw 7.8 and Mw 7.6 earthquake doublet in SE Türkiye, *Seismica* **2,** doi: 10.26443/seismica.v2i3.387.

Milner, K. R., B. E. Shaw, and E. H. Field (2022). Enumerating plausible multifault ruptures in complex fault systems with physical constraints, *Bull. Seismol. Soc. Am.* **112,** no. 4, 1806–1824, doi: 10.1785/0120210322.

Oglesby, D. D., S. M. Day, Y.-G. Li, and J. E. Vidale (2003). The 1999 Hector Mine earthquake: The dynamics of a branched fault system, *Bull. Seismol. Soc. Am.* **93,** no. 6, 2459–2476.

Okuwaki, R., Y. Yagi, T. Taymaz, and S. P. Hicks (2023). Multi-scale rupture growth with alternating directions in a complex fault network during the 2023 South-Eastern Türkiye and Syria earthquake doublet, *Geophys. Res. Lett.* **50,** no. 12, e2023GL103480, doi: 10.1029/2023GL103480.

Perrin, C., I. Manighetti, J. Paul Ampuero, F. Cappa, and Y. Gaudemer (2016). Location of largest earthquake slip and fast rupture controlled by along-strike change in fault structural maturity due to fault growth, *J. Geophys. Res.* doi: 10.1002/2015JB012671.Received.

Poliakov, A. N. B., R. Dmowska, and J. R. Rice (2002). Dynamic shear rupture interactions with fault bends and off-axis secondary faulting, *J. Geophys. Res.* **107,** no. B11, ESE 6-1–ESE 6-18, doi: 10.1029/2001JB000572.

Ramos, M. D., P. Thakur, Y. Huang, R. A. Harris, and K. J. Ryan (2022). Working with dynamic earthquake rupture models: A practical guide, *Seismol. Res. Lett.* **93,** no. 4, 2096–2110.

Rice, J. R. (1992). Chapter 20 fault stress states, pore pressure distributions, and the weakness of the San Andreas Fault, in *Fault Mechanics and Transport Properties of Rocks*, B. Evans and T. F. Wong (Editors), Vol. 51, Academic Press, doi: 10.1016/S0074-6142(08)62835-1.

Saroglu, F. (1992). The East Anatolian fault zone of Turkey, *Ann. Tectonicae* **6,** 99–125.

Sibson, R. (1992). Implications of fault-valve behaviour for rupture nucleation and recurrence, *Tectonophysics* **211,** nos. 1/4, 283–293.

Taufiqurrahman, T., A. A. Gabriel, D. Li, T. Ulrich, B. Li, S. Carena, A. Verdecchia, and F. Gallovič (2023). Dynamics, interactions and delays of the 2019 Ridgecrest rupture sequence, *Nature* **618,** 308–315, doi: 10.1038/s41586-023-05985-x.

Taymaz, T., Y. Yilmaz, and Y. Dilek (2007). *The Geodynamics of the Aegean and Anatolia: Introduction*, Vol. 291, Geological Society, London, Special Publications, London, 1–16, doi: 10.1144/SP291.1.

# Supplemental Material for "3D dynamic rupture modeling of the February 6, 2023, Kahramanmaraş, Turkey, $M_W$ 7.8 and $M_W$ 7.7 earthquake doublet using early observations"

**Alice-Agnes Gabriel[1,2], Thomas Ulrich[2], Mathilde Marchandon[2], James Biemiller[3], John Rekoske[1]**

[1]Scripps Institution of Oceanography, UC San Diego, La Jolla, USA
[2]Department of Earth and Environmental Sciences, Ludwig-Maximillians-Universität München, Germany.
[3]U.S. Geological Survey, Portland, Oregon, USA

**The supplemental material contains Supplementary Tables S1-S3, Supplementary Figures S1-S9, legends for Supplemental Videos S1, S2, S3 & S4, and References.**

Disclaimer: Any use of trade, firm, or product names is for descriptive purposes only and does not imply endorsement by the U.S. Government.

## Supplemental Tables

**Table S1.** We embed all faults in a 1D velocity model adapted from Güvercin et al., 2022, which is similar to the best-performing model for dynamic source inversion using strong-ground motion data of the 2020 Elaziğ earthquake (Gallovič et al., 2020). Plastic cohesion $C_{\text{plast}}$ is set proportional to the 1D depth-dependent shear modulus $\mu(z)$ (in Pa) as $C_{\text{plast}} = 2 \times 10^{-4} \max(\mu(z), 2 \times 10^{10})$ (Roten et al., 2014). We taper bulk cohesion $C_{\text{plast}}$ at depths shallower than 2 km, where confinement stresses are low. The onset of plastic yielding is not instantaneous but governed by viscoplastic relaxation with a relaxation time $T_{\text{v}}$ set to 0.05 s, which ensures convergence of simulation results with mesh refinement (Wollherr et al., 2018).

| Depth [km] | density [$\text{kg m}^{-3}$][a] | $c_S$[km/s][b] | $c_P$[km/s][c] |
|---|---|---|---|
| 1.0 | 2465.0 | 2.43 | 4.52 |
| 2.0 | 2640.2 | 3.03 | 5.62 |
| 4.0 | 2665.2 | 3.31 | 5.75 |
| 6.0 | 2685.3 | 3.38 | 5.85 |
| 8.0 | 2708.1 | 3.43 | 5.96 |
| 10.0 | 2716.7 | 3.44 | 6.0 |
| 12.0 | 2727.5 | 3.46 | 6.05 |
| 16.0 | 2789.0 | 3.62 | 6.32 |
| 20.0 | 2808.3 | 3.67 | 6.4 |
| 25.0 | 2920.1 | 3.92 | 6.83 |
| 30.0 | 2936.8 | 3.94 | 6.89 |
| 37.0 | 3221.2 | 4.4 | 7.8 |
| 45.0 | 3370.6 | 4.56 | 8.22 |
| 1000.0 | 3400.2 | 4.61 | 8.3 |

[a] derived from $c_P$ using the Nafe-Drake curve, Brocher (2005) [b]S-wave speed [c]P-wave speed

**Table S2.**  The 3D dynamic rupture modeling parameters of the preferred scenarios of the February 6, 2023, Kahramanmaraş, Turkey, $M_W 7.8$ and $M_W 7.7$ earthquake doublet using early observations.

| Parameter | Notation | $M_W 7.8$ model | $M_W 7.7$ model |
| --- | --- | --- | --- |
| Static friction coefficient | $\mu_s$ | 0.6 | 0.6 |
| Dynamic friction coefficient | $\mu_d$ | 0.2 | 0.2 |
| Nucleation patch radius | $r_{nuc}$ [km] | 2 | 3 |
| Critical slip weakening distance | $D_c$ [m] | 0.5 | $1.0^a$ |

$^a$ Fault 10 of the $M_W 7.7$ scenario has $D_c$=0.5, see Fig. 1c.

**Table S3.** Sentinel-2 images used to compute the surface displacements of the earthquake doublet. We use Sentinel-2 images (10 m resolution) freely available from the European Space Agency (`https://scihub.copernicus.eu/dhus/#/home`). Height pairs of pre- and post-event images taken in spring 2022, and on May 5, 2023, respectively, are mosaicked to cover the study area. We choose pre- and post-images taken at the same time of the year (i.e., spring) to limit illumination bias in the correlation. We correlate the pre- and post-event images using the phase correlator of the software package COSI-Corr (Ayoub et al., 2009; Leprince et al., 2007; Aati et al., 2022) with a multiscale sliding correlation window of 128 to 64 pixels and a measurement step of 8 pixels. This results in EW and NS displacement fields with a ground sampling of 80 m. We discarded data points with a low signal-to-noise ratio ($< 0.95$) and outliers with displacement amplitudes higher than 15 m. Along-track undulations due to Charge-Coupled Device (CCD) array artifacts were removed by stacking and subtracting the average artifact signal from the correlation. Finally, we smoothed the EW and NS displacement fields using the non-local-mean filter implemented in COSI-Corr (Buades et al., 2005). From the Sentinel-2 horizontal displacement field, we measured the EW and NS fault offsets using regularly spaced fault-perpendicular stacked profiles. We use 16 km long profiles and, to increase the signal-over-noise ratio, we stack them over a width of 4 km. For each profile, the fault offset is then measured by fitting linear regressions to the displacement on each side of the fault and measuring the displacement difference of the linear regressions across the fault. We estimate the error in the estimated fault offsets by the root mean square of the standard deviations (1-sigma) of the linear regression on each side of the fault.

| Sentinel-2 image ID | Date (mm.dd.yy) |
|---|---|
| S2B_MSIL2A_20220530T081609_N0400_R121_T37SBA_20220530T103428 | 05.30.22 |
| S2B_MSIL2A_20220530T081609_N0400_R121_T37SBB_20220530T103428 | 05.30.22 |
| S2B_MSIL2A_20220619T081609_N0400_R121_T37SBC_20220619T102831 | 06.19.22 |
| S2B_MSIL1C_20220530T081609_N0400_R121_T37SCA_20220530T091117 | 05.30.22 |
| S2B_MSIL2A_20220530T081609_N0400_R121_T37SCB_20220530T103428 | 05.30.22 |
| S2B_MSIL2A_20220619T081609_N0400_R121_T37SCC_20220619T102831 | 05.30.22 |
| S2B_MSIL2A_20220530T081609_N0400_R121_T37SDB_20220530T103428 | 05.30.22 |
| S2B_MSIL1C_20220619T081609_N0400_R121_T37SDC_20220619T091128 | 06.19.22 |
| S2B_MSIL2A_20230505T081609_N0509_R121_T37SBA_20230505T095847 | 05.05.23 |
| S2B_MSIL2A_20230505T081609_N0509_R121_T37SBB_20230505T095847 | 05.05.23 |
| S2B_MSIL1C_20230505T081609_N0509_R121_T37SBC_20230505T085532 | 05.05.23 |
| S2B_MSIL2A_20230505T081609_N0509_R121_T37SCA_20230505T095847 | 05.05.23 |
| S2B_MSIL1C_20230505T081609_N0509_R121_T37SCB_20230505T085532 | 05.05.23 |
| S2B_MSIL2A_20230505T081609_N0509_R121_T37SCC_20230505T095847 | 05.05.23 |
| S2B_MSIL2A_20230505T081609_N0509_R121_T37SDB_20230505T095847 | 05.05.23 |
| S2B_MSIL1C_20230505T081609_N0509_R121_T37SDC_20230505T085532 | 05.05.23 |

## Supplemental Figures
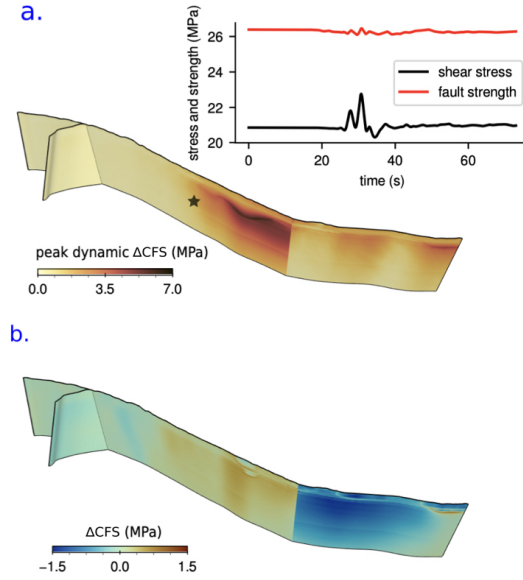


**Figure S1.**   a. Co-seismic and b. post-seismic stress changes of the $M_\mathrm{w}7.8$ dynamic rupture scenario measured on the faults of the $M_\mathrm{w}7.7$ earthquake. By modeling both earthquakes in the same dynamic rupture simulation, we include the constraint that the second earthquake's fault structure is not dynamically triggered during the first earthquake rupture. a. Peak dynamic shear stress perturbation measured in the direction of maximum initial shear traction. Inset: Evolution of dynamic shear stress and fault strength at the $M_\mathrm{w}7.7$ hypocenter (black star). Fault strength is defined as the product of local friction coefficient and effective normal stress; slip would occur when fault strength equals the magnitude of shear traction. b. Static Coulomb failure stress changes ($\Delta$CFS) calculated as: $\Delta\mathrm{CFS}{=}\Delta\tau \ - \ \mu_s\Delta\sigma_n$, $\Delta\tau$ and $\Delta\sigma_n$ are the shear and normal fault stress changes, and $\mu_s = 0.6$ is the static friction coefficient. Despite different relative prestress ratios (fault-local $R$), stress changes are similar to the more heterogeneous dynamic rupture models in Jia et al. (2023) Fig. 4 C,D. In the east, the stress shadow (Harris & Simpson, 1996), i.e. (negative) $\Delta$CFS, is the largest.
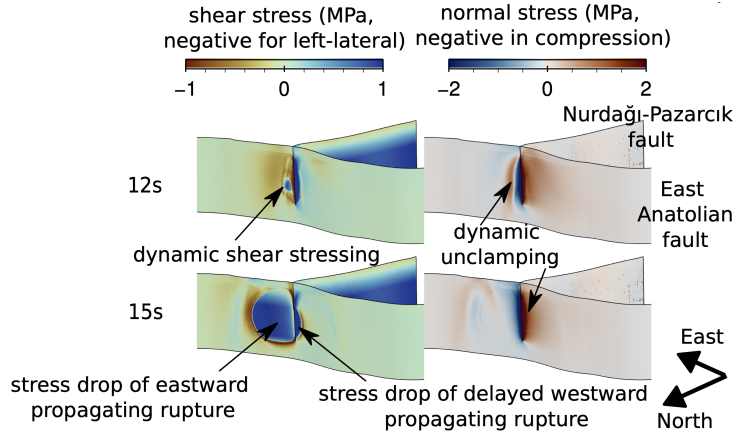
**Figure S2.** Zoom into the NPF-EAF fault intersection at 12 s and 15 s simulation time of the $M_\mathrm{w}7.8$ dynamic rupture scenario (Fig. 3a), illustrating rupture dynamics of overcoming the geometric barrier and delayed branching in the backward direction. Despite different relative prestress ratios (fault-local $R$), this dynamic mechanism is similar to one in the more heterogeneous scenarios, as shown in Fig. S26 in Jia et al. (2023).
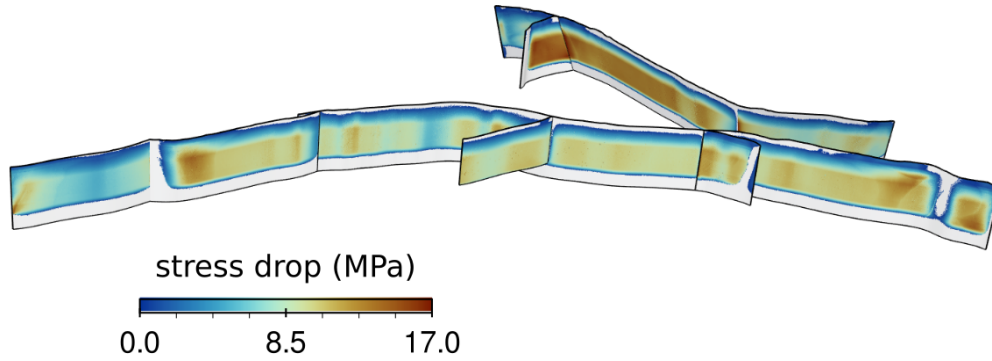


**Figure S3.** Modeled stress drop of both dynamic rupture scenarios. Assuming larger fracture energy (larger $D_c$) and prestress (larger $R_0$ and $SH_\mathrm{max}$) governing the second earthquake in our preferred scenario leads to larger stress drop but not to larger peak ground velocities, see Figs. 4d, S8. We measure on-fault stress drop as the difference between initial shear stress and final shear stress.
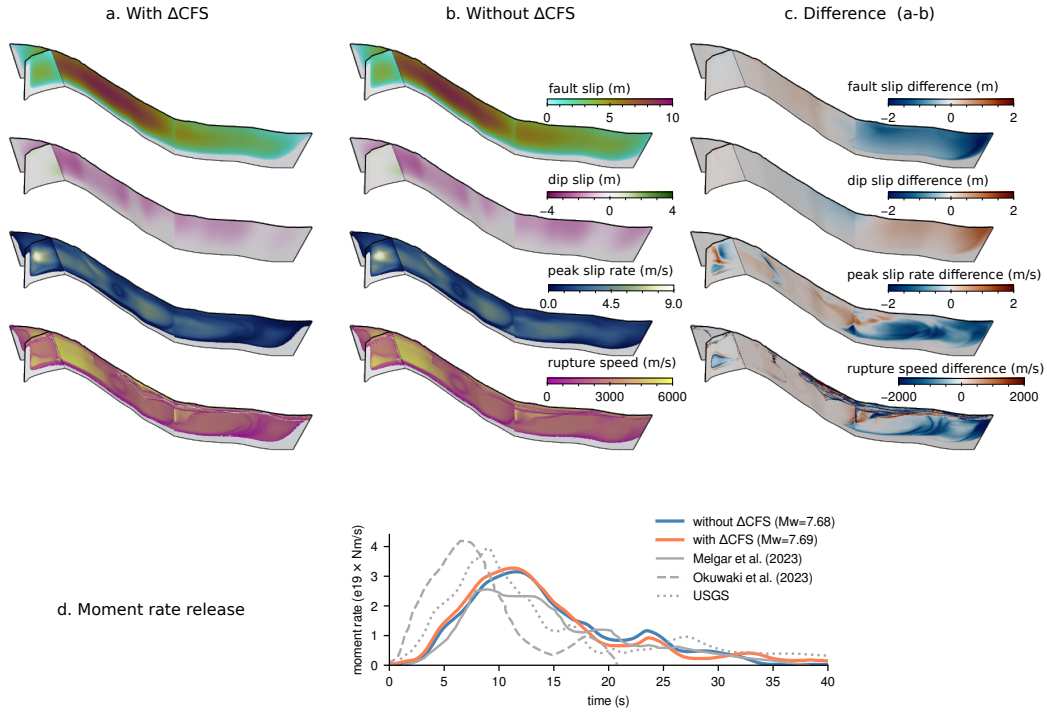
**Figure S4.** a. Effect of static Coulomb failure stress changes ($\Delta CFS$) on the 3D rupture dynamics of the $M_{\mathrm{w}}7.7$ earthquake. b. The dynamic rupture simulation of the $M_{\mathrm{w}}7.7$ earthquake without accounting for $\Delta CFS$ of the first earthquake. c. Difference in rupture dynamics between scenarios with and without the effect of $\Delta CFS$. d.: Comparison of $M_{\mathrm{w}}7.7$ dynamic rupture moment release rates with and without $\Delta CFS$ compared to kinematic models (Goldberg et al., 2023; Melgar et al., 2023; Okuwaki et al., 2023).
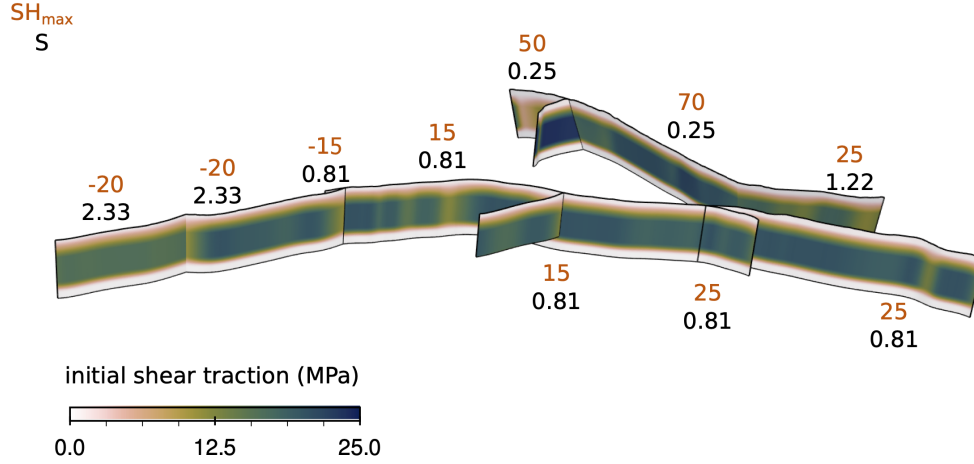
**Figure S5.** Spatial variability of initial conditions for dynamic rupture modeling of both large earthquakes, constrained from newly performed regional stress inversion. $SH_{\max}$ (orange numbers) is the direction of the regional maximum horizontal compressive prestress acting on each fault and varying across the fault system. We use the seismicity reported in Güvercin et al. (2022) to perform a new regional stress tensor inversion. We detail our stress inversion method in a Jupyter Notebook available at `https://zenodo.org/doi/10.5281/zenodo.10058942`. We use a standard approach following (Michael, 1984; Vavryčuk, 2014) to invert stress from focal mechanisms. Our results yield $\nu \approx 0.5$, reflecting local strike-slip faulting and variable direction of $SH_{\max}$. The stress shape ratio $\nu$ describes different faulting mechanisms depending on the eigenvalues ($S_1$, $S_2$, and $S_3$; ordered from most compressional to most tensional) of the ambient stress tensor $S_{ij}$, with $\nu = \frac{S_2 - S_3}{S_1 - S_3}$. We assume that the ambient prestress is 3D heterogeneous and always Andersonian (Anderson, 1905), i.e. one principal stress component ($S_2$) is vertical. When $S_2$ is vertical, $\nu < 0.5$ characterizes a transpressional regime, $\nu = 0.5$ characterizes a pure strike-slip regime, and $\nu > 0.5$ characterizes a transtensional regime. $S$ (black numbers) is the ratio of initial strength excess to nominal stress drop and a measure of the relative strength of each fault segment related to the relative prestress ratio $R_0$ (Fig. 1c) as $S = 1/(R_0 - 1)$. We here show the $S$-ratio to illustrate that the same ambient regional prestress ($SH_{\max}$) has been used as in Jia et al., 2023 (their Fig. S20), who superimposed additional small-scale initial condition heterogeneity constrained from a static slip model that led to locally higher S-ratios.
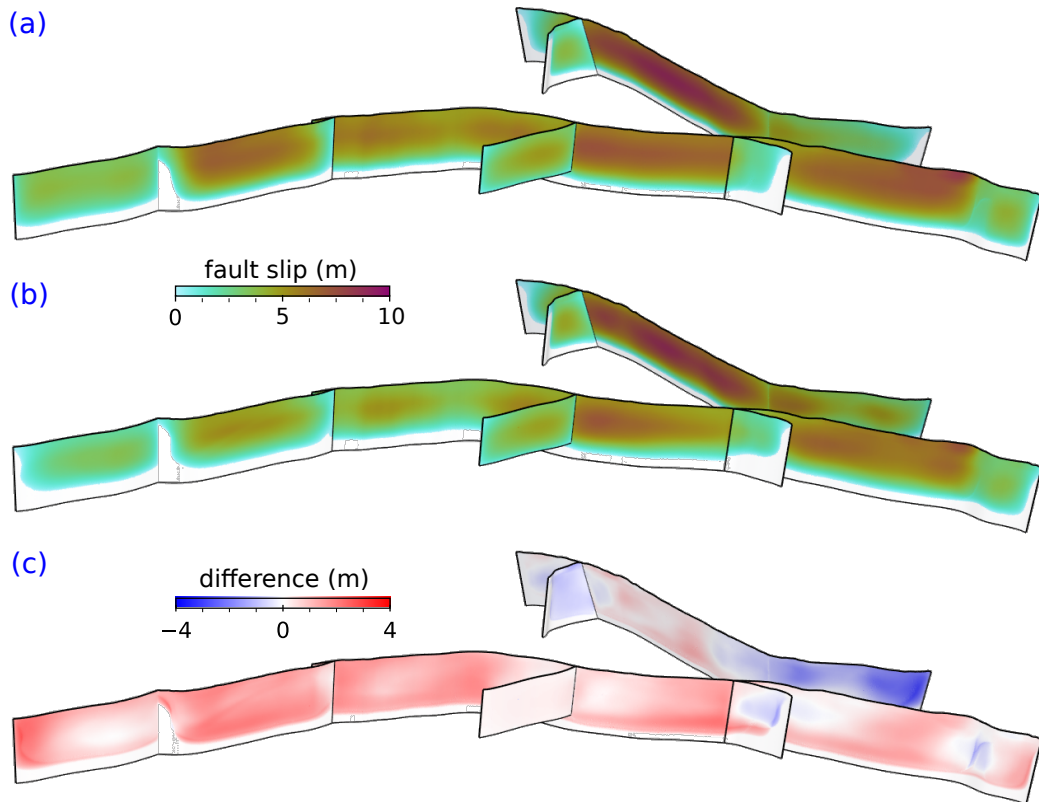
**Figure S6.** Comparison of slip distributions of linked dynamic rupture simulations of both earthquakes. Top: Simple dynamic rupture scenarios. Middle: Refined dynamic rupture scenarios (Jia et al., 2023). Bottom: Difference in slip distribution. The simple dynamic rupture scenario results in a slightly higher geodetic misfit than the more heterogeneous dynamic rupture scenario (maximum misfit increase of 2.2% for the SAR azimuth data).
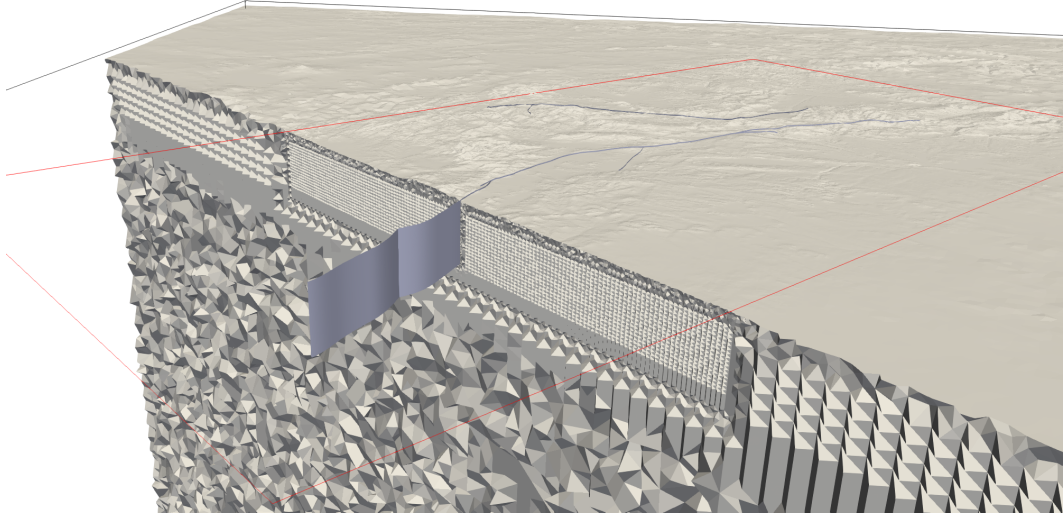
**Figure S7.** Cut-out view of the computational mesh, including fault surface traces and surfaces in grey and the outline of the high-resolution area in red. The model domain used to simulate both earthquakes jointly accounts for high-resolution (450 m) topography data from the Shuttle Radar Topography Mission (SRTM) Digital Elevation Model (DEM) (Farr et al., 2007). The mesh, acknowledging the 1D velocity model, is statically adapted to resolve frequencies of at least 1 Hz in the high-resolution area and at least 0.25 Hz elsewhere. We use this mesh to solve the spontaneous dynamic rupture and seismic wave propagation problem using the open-source software SeisSol (`https://github.com/SeisSol/SeisSol`). SeisSol uses the Arbitrary high-order accurate DERivative Discontinuous Galerkin method (ADER-DG, Dumbser & Käser (2006)) and end-to-end optimization for high-performance computing infrastructure (Breuer et al., 2014; Heinecke et al., 2014; Rettenberger et al., 2016; Uphoff et al., 2017; Krenz et al., 2021). SeisSol is verified in a wide range of community benchmarks (Pelties et al., 2014) by the SCEC/USGS Dynamic Rupture Code Verification project (Harris et al., 2018). The spatially adaptive mesh resolution is set to an element edge length of $h = 300$ m close to all faults and gradually coarsened away from the fault surfaces. We define a high-resolution part of our model, which is a $400 \times 200 \times 25$ km cube with edges aligned NE, NW, and up-down. It includes the complete fault systems and most local strong motion stations. We use a custom transverse Mercator projection defined by the PROJ.4 string "+proj=tmerc +datum=WGS84 +k=0.9996 +lon_0=37 +lat_0=37". We statically adapt mesh resolution always to resolve frequencies of at least 1 Hz within the high-resolution area, acknowledging the 1D seismic velocity model. To this end, we require 3 elements to resolve the seismic wavefield sufficiently. We use high-order basis functions of polynomial degree $p = 4$, leading to a 5th-order space-time accurate numerical scheme for wave propagation. The constructed unstructured tetrahedral mesh consists of 31 million elements. Simulating 300 seconds of physical simulation time on this computational mesh requires 20k CPU hours on the Skylake SuperMUC-NG supercomputer (Leibniz Supercomputing Center, Germany). The size of the area behind the rupture front in which shear stress decreases from its static to its dynamic value is the process zone width. In the dynamic rupture models presented, we measure the median process zone width as 670 m, while 95% of the ruptured fault elements are larger than 325 m. Our rupture models are well resolved (Day et al., 2005) by our chosen discretization of $h = 300$ m, noting that each dynamic rupture element provides sub-element-resolution (Wollherr et al., 2018).
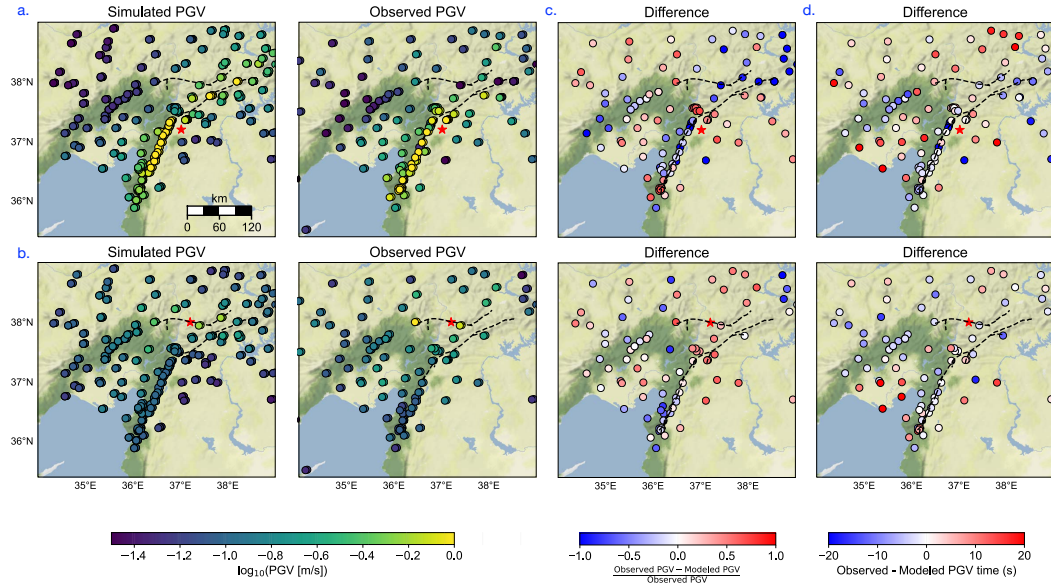
**Figure S8.** a.,b. Same as Fig. 4c,d but color-coded by PGV amplitude. Maps of the observed and simulated PGV measurements (AFAD), at unclipped strong motion stations that recorded the $M_w7.8$ (top) and $M_w7.7$ earthquakes (bottom). We obtained strong ground motion data from the Turkish National Strong Motion Network through the Disaster and Emergency Management Presidency of Turkey (AFAD, `https://tadas.afad.gov.tr`). c. Relative difference of observed and modeled PGV amplitudes for both earthquakes. d. Absolute difference of observed and modeled PGV timing for both earthquakes. Colormaps are saturated.
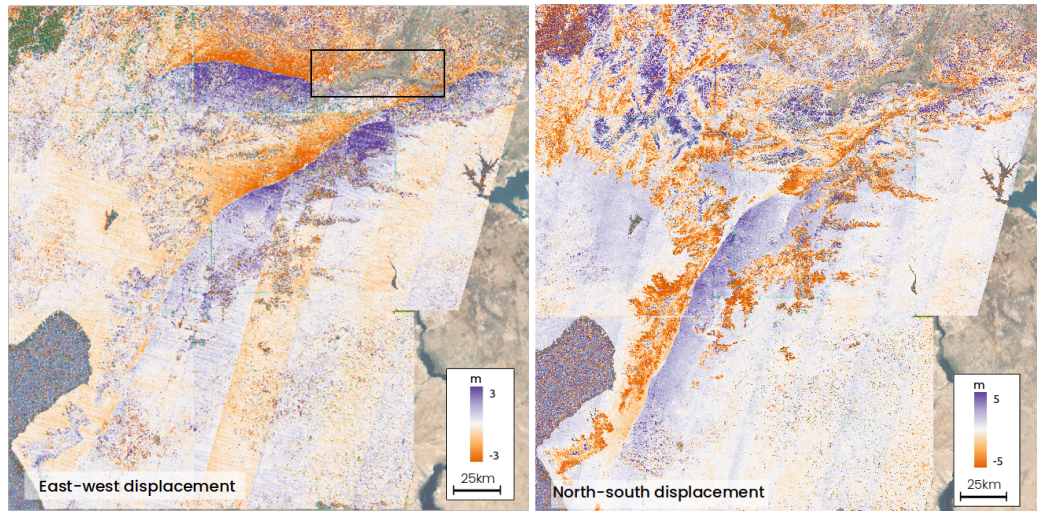


**Figure S9.** First version of the Sentinel-2 optical displacement field obtained 3 days after the doublet. The black rectangle highlights the only part of the rupture (along the Malatya segment) that we were not able to map using these preliminary optical data. The Sentinel-2 optical images are freely available and were downloaded from the European Space Agency website (`https://scihub.copernicus.eu/dhus/#/home`).

## Supplemental Videos

Video S1: Slip rate animation, dynamic rupture scenario of the $M_W$ 7.8 earthquake.

Video S2: Slip rate animation, dynamic rupture scenario of the $M_W$ 7.7 earthquake.

Video S3: Combined seismic wave field and slip rate animation, dynamic rupture scenario of the $M_W$ 7.8 earthquake.

Video S4: Combined seismic wave field and slip rate animation, dynamic rupture scenario of the $M_W$ 7.7 earthquake.

## References

Aati, S., Milliner, C., & Avouac, J.-P. (2022). A new approach for 2-D and 3-D precise measurements of ground deformation from optimized registration and correlation of optical images and ICA-based filtering of image geometry artifacts. *Remote Sensing of Environment, 277*, 113038.

Anderson, E. M. (1905). The dynamics of faulting. *Trans. Edinburgh Geol. Soc, 8*(3), 387-402. doi: 10.1144/transed.8.3.387

Ayoub, F., Leprince, S., & Keene, L. (2009). User's guide to COSI-CORR co-registration of optically sensed images and correlation. *California Institute of Technology: Pasadena, CA, USA, 38*, 49s.

Breuer, A., Heinecke, A., Rettenberger, S., Bader, M., Gabriel, A.-A., & Pelties, C. (2014). Sustained Petascale Performance of Seismic Simulations with SeisSol on SuperMUC. In *Supercomputing. ISC 2014. Lecture Notes in Computer Science, vol 8488* (p. 1-18). Springer. doi: 10.1007/978-3-319-07518-1_1

Brocher, T. M. (2005). Empirical relations between elastic wavespeeds and density in the Earth's crust. *Bulletin of the Seismological Society of America, 95*(6), 2081–2092. doi: 10.1785/0120050077

Buades, A., Coll, B., & Morel, J.-M. (2005). A non-local algorithm for image denoising. In *2005 IEEE Computer Society Conference on Computer Vision and Pattern Recognition (CVPR'05)* (Vol. 2, pp. 60–65). IEEE. doi: 10.1109/CVPR.2005.38

Day, S. M., Dalguer, L. A., Lapusta, N., & Liu, Y. (2005). Comparison of finite difference and boundary integral solutions to three-dimensional spontaneous rupture. *Journal of Geophysical Research: Solid Earth, 110*(B12). doi: 10.1029/2005JB003813

Dumbser, M., & Käser, M. (2006). An arbitrary high-order discontinuous Galerkin method for elastic waves on unstructured meshes—II. The three-dimensional isotropic case. *Geophysical Journal International, 167*(1), 319–336. doi: 10.1111/j.1365-246X.2006.03120.x

Farr, T. G., Rosen, P. A., Caro, E., Crippen, R., Duren, R., Hensley, S., ... Alsdorf, D. (2007). The Shuttle Radar Topography Mission. *Rev. Geophys., 45*(2), RG2004. doi: 10.1029/2005RG000183

Gallovič, F., Zahradník, J., Plicka, V., Sokos, E., Evangelidis, C., Fountoulakis, I., & Turhan, F. (2020). Complex rupture dynamics on an immature fault during the 2020 Mw 6.8 Elazığ earthquake, Turkey. *Communications Earth & Environment, 1*(1), 40.

Goldberg, D. E., Taymaz, T., Reitman, N. G., Hatem, A. E., Yolsal-Çevikbilen, S., Barnhart, W. D., ... Altuntaş, C. (2023). Rapid characterization of the February 2023 Kahramanmaraş, Türkiye, earthquake sequence. *The Seismic Record, 3*(2), 156-167. doi: 10.1785/0320230009

Güvercin, S. E., Karabulut, H., Konca, A. Ö., Doğan, U., & Ergintav, S. (2022). Active seismotectonics of the East Anatolian Fault. *Geophysical Journal International, 230*(1), 50–69.

Harris, R. A., Barall, M., Aagaard, B., Ma, S., Roten, D., Olsen, K., . . . Dalguer, L. (2018). A suite of exercises for verifying dynamic earthquake rupture codes. *Seismol. Res. Lett.*, *89*(3), 1146-1162. doi: 10.1785/0220170222

Harris, R. A., & Simpson, R. W. (1996). In the shadow of 1857 – the effect of the great Ft. Tejon earthquake on subsequent earthquakes in southern California. *Geophysical Research Letters*, *23*(3), 229–232.

Heinecke, A., Breuer, A., Rettenberger, S., Bader, M., Gabriel, A. A., Pelties, C., . . . Dubey, P. (2014). Petascale high order dynamic rupture earthquake simulations on heterogeneous supercomputers. In *SC'14: International Conference for High-Performance Computing, Networking, Storage and Analysis.* doi: doi.org/10.1109/SC.2014.6

Jia, Z., Jin, Z., Marchandon, M., Ulrich, T., Gabriel, A.-A., Fan, W., . . . Fialko, Y. (2023). The complex dynamics of the 2023 Kahramanmaras, Turkey, Mw 7.8-7.7 earthquake doublet. *Science*, *381*(6661), 985-990. doi: 10.1126/science.adi0685

Krenz, L., Uphoff, C., Ulrich, T., Gabriel, A.-A., Abrahams, L., Dunham, E., & Bader, M. (2021). 3D acoustic-elastic coupling with gravity: the dynamics of the 2018 Palu, Sulawesi earthquake and tsunami. In *Proceedings of the International Conference for High-Performance Computing, Networking, Storage and Analysis.* New York, NY, USA: ACM. doi: 10.1145/3458817.3476173

Leprince, S., Ayoub, F., Klinger, Y., & Avouac, J.-P. (2007). Co-Registration of Optically Sensed Images and Correlation (COSI-Corr): An operational methodology for ground deformation measurements. In *2007 IEEE International Geoscience and Remote Sensing Symposium* (pp. 1943–1946). IEEE. doi: 10.1109/IGARSS.2007.4423207

Melgar, D., Taymaz, T., Ganas, A., Crowell, B. W., Öcalan, T., Kahraman, M., . . . others (2023). Sub-and super-shear ruptures during the 2023 Mw 7.8 and Mw 7.6 earthquake doublet in SE Türkiye. *Seismica*, *2*. doi: 10.26443/seismica.v2i3.387

Michael, A. J. (1984). Determination of stress from slip data: Faults and folds. *Journal of Geophysical Research: Solid Earth*, *89*(B13), 11517–11526.

Okuwaki, R., Yagi, Y., Taymaz, T., & Hicks, S. P. (2023). Multi-Scale Rupture Growth With Alternating Directions in a Complex Fault Network During the 2023 South-Eastern Türkiye and Syria Earthquake Doublet. *Geophysical Research Letters*, *50*(12), e2023GL103480. doi: 10.1029/2023GL103480

Pelties, C., Gabriel, A.-A., & Ampuero, J.-P. (2014). Verification of an ADER-DG method for complex dynamic rupture problems. *Geoscientific Model Development*, *7*(3), 847-866. doi: 10.5194/gmd-7-847-2014

Rettenberger, S., Meister, O., Bader, M., & Gabriel, A.-A. (2016). ASAGI: A Parallel Server for Adaptive Geoinformation. In *Proceedings of the exascale applications and software conference 2016* (p. 2:1-2:9). New York, NY, USA: ACM. doi: 10.1145/2938615.2938618

Roten, D., Olsen, K. B., Day, S. M., Cui, Y., & Fäh, D. (2014). Expected seismic shaking in Los Angeles reduced by San Andreas fault zone plasticity. *Geophys. Res. Lett.*, *41*(8), 2769-2777. doi: 10.1002/2014GL059411

Uphoff, C., Rettenberger, S., Bader, M., Madden, E., Ulrich, T., Wollherr, S., & Gabriel, A.-A. (2017). Extreme scale multi-physics simulations of the tsunamigenic 2004 Sumatra megathrust earthquake. In *Proceedings of the International Conference for High Performance Computing, networking, Storage and Analysis, SC 2017.* doi: 10.1145/3126908.3126948

Vavryčuk, V. (2014). Iterative joint inversion for stress and fault orientations from focal mechanisms. *Geophysical Journal International*, *199*(1), 69-77. doi: 10.1093/gji/ggu224

Wollherr, S., Gabriel, A.-A., & Uphoff, C. (2018). Off-fault plasticity in three-dimensional dynamic rupture simulations using a modal Discontinuous Galerkin method on unstructured meshes: Implementation, verification and application.

Wang, Z., W. Zhang, T. Taymaz, Z. He, T. Xu, and Z. Zhang (2023). Dynamic rupture process of the 2023 Mw 7.8 Kahramanmaraş earthquake (SE Türkiye): Variable rupture speed and implications for seismic hazard, *Geophys. Res. Lett.* **50,** no. 15, e2023GL104787, doi: 10.1029/2023GL104787.

Weiss, J. R., R. J. Walters, Y. Morishita, T. J. Wright, M. Lazecky, H. Wang, E. Hussain, A. J. Hooper, J. R. Elliott, C. Rollins, *et al.* (2020). High-resolution surface velocities and strain for Anatolia from Sentinel-1 InSAR and GNSS data, *Geophys. Res. Lett.* **47,** no. 17, e2020GL087376, doi: 10.1029/2020GL087376.

Wollherr, S., A.-A. Gabriel, and P. M. Mai (2019). Landers 1992 "reloaded": Integrative dynamic earthquake rupture modeling, *J. Geophys. Res.* **124,** no. 7, 6666–6702.